Amphiphilic Dendrimer Doping Enhanced pH-Sensitivity of Liposomal Vesicle for Effective Co-delivery Toward Synergistic Ferroptosis-Apoptosis Therapy of Hepatocellular Carcinoma

Yanhong Su, Zhao Zhang, Leo Tsz, Ling Peng, Ligong Lu, Xu He, Xuanjun Zhang

To cite this version:

Yanhong Su, Zhao Zhang, Leo Tsz, Ling Peng, Ligong Lu, et al.. Amphiphilic Dendrimer Doping Enhanced pH-Sensitivity of Liposomal Vesicle for Effective Co-delivery Toward Synergistic Ferroptosis-Apoptosis Therapy of Hepatocellular Carcinoma. Advanced Healthcare Materials, 2023, 12 (6), pp.2202663. ⟨10.1002/adhm.202202663⟩. ⟨hal-03940472⟩

HAL Id: hal-03940472
https://hal.science/hal-03940472v1

Amphiphilic Dendrimer Doping Enhanced pH-Sensitivity of Liposomal Vesicle for Effective Co-delivery Toward Synergistic Ferroptosis–Apoptosis Therapy of Hepatocellular Carcinoma

Yanhong Su+[a,b] Zhao Zhang+[a], Leo Tsz On LEE[a,d], Ling Peng[c], Ligong Lu*[b], Xu He*[b], Xuanjun Zhang*[a,d]
+These authors contributed equally to this work

[a] Y. Su, Z. Zhang, Prof. L. T. O. Lee, Prof. X. Zhang
Faculty of Health Sciences
University of Macau, Taipa, Macau 999078, China
E-mail: xuanjunzhang@um.edu.mo (X. Zhang)
[b] Dr. Y. Su, Prof. L. Lu, Dr. X. He
Guangdong Provincial Key Laboratory of Tumor Interventional Diagnosis and Treatment
Zhuhai People's Hospital (Zhuhai Hospital Affiliated with Jinan University)
Zhuhai, 519000, Guangdong, China
E-mail: luligong1969@jnu.edu.cn (L. Lu)
E-mail: hexu220@163.com (X. He)
[c] Dr. L. Peng
Aix Marseille Université
CNRS
Centre Interdisciplinaire de Nanoscience de Marseille (CINaM), UMR 7325
Equipe Labellisée Ligue Contre le Cancer
Marseille 13288, France
[d] Prof. L. T. O. Lee, Prof. X. Zhang
MOE Frontiers Science Centre for Precision Oncology
University of Macau, Taipa, Macau 999078, China

Abstract: Ferroptosis, characterized by the accumulation of reactive oxygen species and lipid peroxides, has emerged as an attractive strategy to reverse drug resistance. Of particular interest is the ferroptosis–apoptosis combination therapy for cancer treatment. Herein, we report a nanoplatform for effective co-delivery of the anticancer drug sorafenib (S) and the ferroptosis inducer hemin (H) toward synergistic ferroptosis–apoptosis therapy of advanced hepatocellular carcinoma (HCC) as a proof-of-concept study. Liposome is an excellent delivery system; however, it is not sufficiently responsive to the acidic tumor microenvironment (TME) for tumor-targeted drug delivery. We therefore developed pH-sensitive vesicles (SH-AD-L) by incorporating amphiphilic dendrimers (AD) into liposomes for controlled and pH-stimulated release of sorafenib and hemin in the acidic TME, thanks to the protonation of numerous amine functionalities in AD. Importantly, SH-AD-L not only blocked glutathione synthesis to disrupt the antioxidant system but also increased intracellular Fe2+ and •OH concentrations to amplify oxidative stress, both of which contribute to enhanced ferroptosis. Remarkably, high levels of •OH also augmented sorafenib-mediated apoptosis in tumor cells. This study demonstrates the power and efficacy of the effective ferroptosis–apoptosis combination therapy, as well as the promise of the AD-doped TME-responsive vesicles for drug delivery in combination therapy to treat advanced HCC.

Introduction

Cancer is a global health problem. Almost all drugs used in cancer chemotherapy trigger apoptosis for their anticancer activity [1]. Overall, the efficacy of the current anticancer drugs is far from satisfactory due to the intrinsic apoptosis-resistance of tumor cells [2]. Therefore, exploring non-apoptotic treatment modalities for effective tumor suppression is of urgent importance. Ferroptosis, a form of programmed cell death characterized by iron-dependent lipid peroxide (LPO) accumulation [3] is fundamentally distinct from apoptosis, offering a new opportunity for elaborating therapy to treat the apoptosis-resistant tumor [4]. Ferroptosis is mainly driven by the abnormally high level of intracellular Fe^{2+}. Fe^{2+}, as a redox-active metal ion, is regarded as an attractive ferroptosis inducer to convert high concentrations of H_2O_2 to •OH through the Fenton reaction and initiate lipid peroxidation [5], which can damage the cell membrane integrity, leading to anticancer effect. However, glutathione peroxidase (GPX4), a cellular lipid repair enzyme, can detoxify LPO to nontoxic lipid alcohols using glutathione (GSH) as a reducing cofactor to protect cells from lipid peroxidation [6]. Consequently, it is of great significance if we can amplify oxidative stress by increasing the cellular labile iron pool through iron overloading, and at the same time, destroy the antioxidant defense system through inactivation of GPX4, turning cancer cells more vulnerable to ferroptosis, thereby achieving more effective anticancer potency. In this study, we propose anticancer treatment based on such combination using liver cancer as the cancer model for the proof-of-concept study.

Liver cancer is a challenging cancer to treat, with the incidence and mortality ranking sixth and third, respectively, among tumor-related diseases [7]. Due to the pathogenesis of liver cancer being insidious with rapid progression, most patients are diagnosed at an advanced stage.

Sorafenib is widely used as the first-line therapy for advanced hepatocellular carcinoma (HCC) [8]. However, given that the liver is a metabolic organ participating in glucose, amino acids, and lipid metabolism in the human body, the metabolic disturbance and ROS inhibition triggered to keep redox balance can protect tumor cells from damage when they are treated with traditional chemotherapy drugs [9]. It is reported that the median overall survival is only extended by 2-3 months after treatment with sorafenib [10]. In addition, many patients cannot tolerate the side effects induced by sorafenib, while others do not respond to sorafenib therapy effectively [11]. It is therefore of the utmost urgency to explore a strategy to improve sorafenib responses against advanced HCC. Emerging research suggests that activating ferroptosis may suppress tumor growth and sensitize HCC cells to chemotherapy [12]. Interestingly, sorafenib has been reported to be a better inducer of ferroptosis than induction of apoptosis [13]. Ferroptosis events including GSH depletion, Fe^{2+} overloading, and enhanced lipid ROS concentration appeared in sorafenib-treated HCC cells [14]. Therefore, promoting sorafenib-induced ferroptosis may be a promising therapeutic strategy for HCC treatment [15].

The ferroptosis-related pathways include •OH overproduction and Fe^{2+} overloading. Compounds that can overload Fe^{2+} and overproduce •OH are potent candidates to induce ferroptosis. Hemin, a Fe-containing porphyrin approved by the U.S. Food and Drug Administration for treating acute intermittent porphyria [16], can activate heme oxygenase 1 (HMOX-1) to degrade heme into Fe^{2+} [17], hence enhancing the labile iron pool for potential ferroptosis. In addition, hemin can also be used as an iron catalyst to react with the over-expressed H_2O_2, promoting lipid peroxidation for ferroptosis. In short, hemin can induce tumor cell ferroptosis independent of GSH deprivation [18]. Fe^{2+}overloading and •OH overproduction induced by hemin can bypass the apoptosis resistance and enhance the therapeutic efficacy of traditional therapy [19], exhibiting great potential in catalytic therapy and ferroptosis induction for cancer therapy. In this study, we propose a combination based on hemin with sorafenib for treating advanced HCC, because we expected that hemin could synergize with sorafenib to disturb redox homeostasis in HCC cells by triggering iron overload, •OH production, and GSH depletion, which are crucial for aggravating lipid peroxidation, hence constituting a high-performance strategy to increase the efficacy of sorafenib and further fight against advanced HCC.

For realizing the combination effect of sorafenib and hemin, it is important to have a carrier system to co-deliver them simultaneously to the tumor lesion. Ideal drug delivery systems should respond to the tumor microenvironment to allow for specific and effective drug release within tumor tissue [20]. Among various drug delivery systems developed against cancer, liposomes are the most advanced, with the unique ability to load both hydrophobic and hydrophilic drugs. However, liposomes are, in general, relatively insensitive to pH variation, and hence remain stable in the acidic tumor microenvironment [21]. In variation to liposomes, dendrimersomes composed of amphiphilic dendrimers with abundant amine functionalities are sensitive to pH change and prone to structural rearrangements [22]. This is because numerous amine functionalities in dendrimers can be progressively protonated, hence responding sensitively to different pH variations [22a, 22c, 23].

Inspired by the pH-responsive feature of amphiphilic dendrimers, we envisioned an innovative pH-sensitive hybrid liposomal vesicle consisting of liposomes and the amphiphilic dendrimer (AD), called SH-AD-L, as the carrier to co-deliver sorafenib and hemin for treating advanced HCC. Specifically, we constructed a series of SH-AD-L vesicles based on 1,2-dipalmitoyl-sn-glycero-3-phosphocholine (DPPC), 1,2-distearoyl-sn-glycero-3-phosphoethanolamine-N- [methoxy (polyethylene glycol)-2000] (DSPE-PEG$_{2000}$), cholesterol, and AD. The doping ratio of AD was fine-tuned to select an optimal ratio of sorafenib and hemin co-encapsulation for pH-responsive drug release and amplified oxidative stress-induced ferroptosis and apoptosis (Figure 1). Indeed, hemin triggered Fe^{2+} overloading and produced a massive amount of poisonous •OH in tumors, leading to the amplification of oxidative stress and sensitizing the tumor to sorafenib-induced apoptosis and ferroptosis. The synergistic effect of sorafenib and hemin was systematically assessed both *in vitro* and *in vivo*, supporting the use of pH-sensitive SH-AD-L vesicles for their co-delivery to induce ferroptosis-apoptosis within the tumor microenvironment for effective anticancer potency.

Results and Discussion

We first studied the synergetic effect of hemin and sorafenib on SMMC7721 cells using cytotoxicity assessment with four different weight ratios of sorafenib/hemin (1:0.125, 1:0.25, 1:0.5, and 1:1), and analyzed the combination index values (CI) [24]. Obviously, Hemin alone was almost non-toxic to HCC cells. However, when combined with sorafenib, hemin considerably enhanced the cytotoxicity of sorafenib (Figure S1), In addition, the combination index values were 0.832, 0.776, 0.778, and 0.508, respectively, for the four different weight ratios of sorafenib/hemin (1:0.125, 1:0.25, 1:0.5, and 1:1), highlighting a synergetic effect of sorafenib and hemin combination (Table S1). Also, the half-maximal inhibitory concentrations (IC_{50}) were decreased in the four different weight ratios of sorafenib/hemin, with cytotoxicity being up to the maximal in the sorafenib/hemin ratio of 1:1. We therefore used the sorafenib/hemin ratio of 1:1 for liposomal vesicles preparation.

We then constructed the pH-sensitive AD-L nanoparticles for the co-delivery of sorafenib and hemin as shown in Figure 1. The amphiphilic dendrimer AD bearing a hydrophobic lipid part and hydrophilic polyamidoamine (PAMAM) dendron, was synthesized according to the reported protocol [25]. We prepared a series of liposomal vesicles with different molar ratios of AD alongside DPPC, cholesterol, and DSPE-PEG$_{2000}$ using thin-film hydration. The resulting hybrid liposomal vesicles were named AD$_n$-L (n = 0, 1, 3, 5, 8, 10), where n represents the molar ratio of AD during the preparation process; the molar ratios of DPPC, cholesterol, and DSPE-PEG$_{2000}$ were kept constant (AD: DPPC: cholesterol: DSPE-PEG$_{2000}$= n: 41.7: 8.3: 2.9, mol: mol).

The size, size distribution, polydispersity index (PDI), and zeta potential of AD$_n$-L were evaluated using dynamic light scattering (DLS) analysis. The average sizes were 155, 159, 132, 121, and 151 nm for AD$_0$-L, AD$_1$-L, AD$_3$-L, AD$_5$-L, AD$_8$-L, and AD$_{10}$-L, respectively. Interestingly, at the ratio of AD = 3, the liposomal vesicles were the least polydisperse, hence had the lowest PDI (Figure 2A and S2). The zeta potential of AD$_0$-L was negative, whereas the zeta potentials of AD$_1$-L, AD$_3$-L, AD$_5$-L, AD$_8$-L, and AD$_{10}$-L were positive and increased as the AD molar ratio increased owing to the presence of numerous amino groups in AD (Figure 2B). Based on the excellent dispersion and close-to-neutral potential, we chose AD$_3$-L as the optimum candidate for subsequent studies. AD$_3$-L, hereafter simply referred to as AD-L, was used throughout this manuscript for simplicity.

As the combination of sorafenib and hemin at the molar ratio of 1:1 showed the maximal efficacy, we therefore co-loaded sorafenib and hemin at this molar ratio into the AD-L vesicles, which were referred to as SH-AD-L nanoparticles. The so-formed SH-AD-L nanoparticles had a hollow spherical structure with an average diameter of approximately 100 nm, as revealed by results obtained using DLS and transmission electron microscopy (TEM) (Figure 2C and S4). Also, the successful encapsulation of hemin and sorafenib was illustrated by the UV-vis spectra of SH-AD-L nanoparticles, as we observed a hemin-featured peak at 390 nm and a sorafenib-featured peak at 270 nm (Figure 2D). The drug loading capacity was approximately 7.49% for sorafenib and 2.00% for hemin, according to the standard quantification curves established using the UV-vis absorption spectra (Figure S5). In addition, the SH-AD-L nanoparticles were very stable not only in PBS buffer at pH 7.4 but also in cell culture media DMEM and RPMI-1640, as well (Figure 2E). However, the SH-AD-L nanoparticles were not stable at pH 5.5 and pH 6.5, and their size expanded and became obviously larger (Figure 2F). As a control, AD_0-L and SH-L (SH-AD_0-L) showed stable performance in solution at pH 7.4, pH 6.5, and pH 5.5 (Figure S6). This phenomenon can be explained by a previous report on AD-based nanoparticles for drug delivery: a large amount of amine functionalities in the PAMAM dendron are prone to protonation under acidic conditions and generate electrostatic repulsion, hence expanding the NPs in size and accelerating drug release [22c]. We further studied the drug release profiles of SH-AD-L and SH-L at pH 5.5. Effectively, the sorafenib release from SH-AD-L was obviously promoted at pH 5.5, reaching 83% within 24h, whereas SH-L displayed only moderate release (Figure S7). This highlights that AD doping is important, and it can effectively enhance the pH sensitivity of liposomal vesicles and promote drug release.

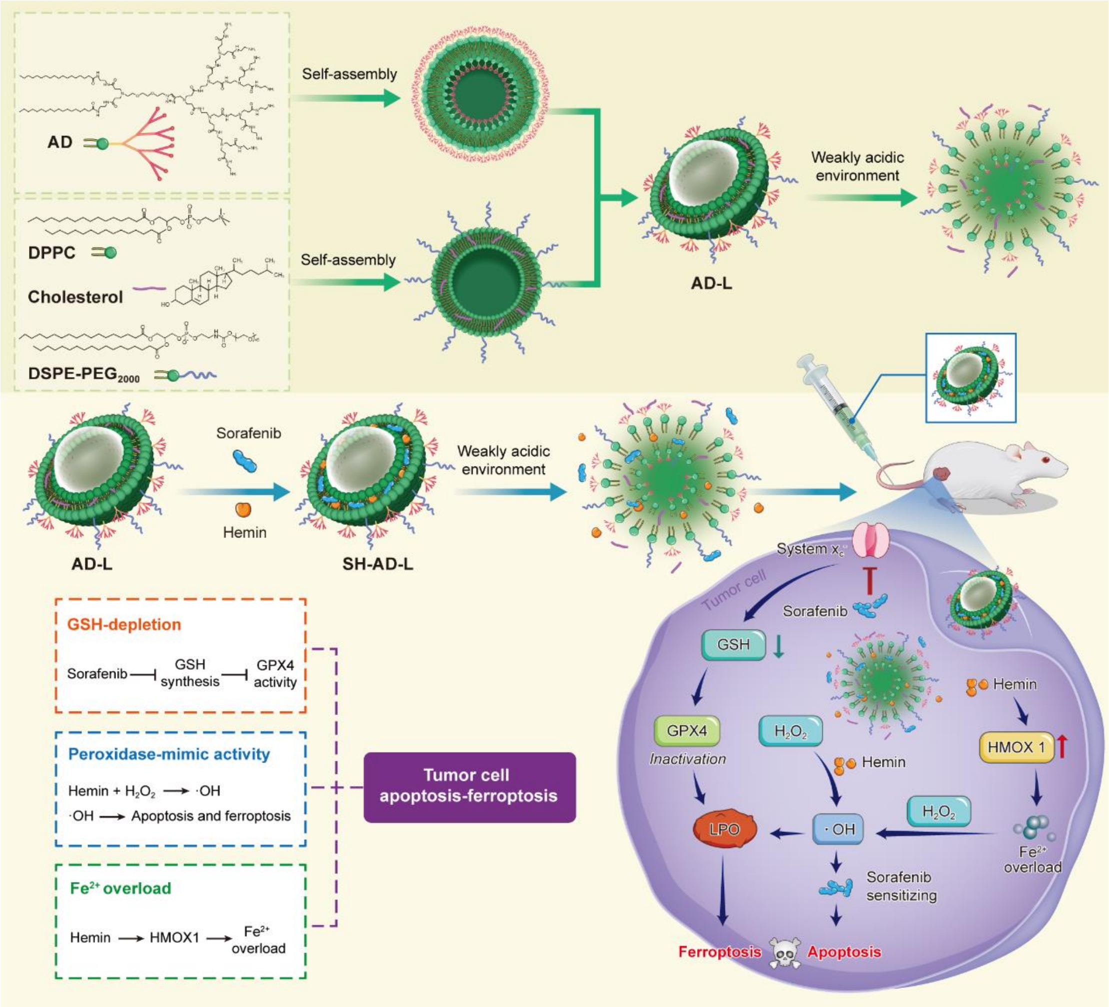

Figure 1. Schematic of the SH-AD-L liposomal vesicle for synergistic ferroptosis-apoptosis against advanced hepatocellular carcinoma.

In order to verify whether SH-AD-L nanoparticles retain the properties of hemin to catalyze H_2O_2 to •OH in acidic tumor microenvironments for lipid peroxidation, we first assessed its peroxidase (POD)-mimic catalytic activity. We used 3,3',5,5'-tetramethylbenzidine (TMB) as a chromomeric substrate, and hydroxyphenyl fluorescein (HPF) as a fluorescent probe to monitor •OH production (Figure 3A). Specifically, SH-AD-L nanoparticles reacted with H_2O_2 to produce •OH, which not only catalyzed the oxidation of colorless TMB to blue-colored oxidized TMB (oxTMB) with two typical absorbance peaks at 370 and 650 nm, but also oxidized nonfluorescent HPF to yield bright green fluorescence (maximum emission: 515 nm). The catalytic activity of SH-AD-L nanoparticles was assessed at different pH conditions in order to simulate the normal physiological environment (pH = 7.4) and the acidic tumor microenvironment (pH = 5.5 and 6.5). The optimal catalytic activity was observed at pH 5.5 (Figure 3B). This is in line with the POD-mimic activity, which is favored in acidic conditions [26]. Hence, all subsequent catalytic analyses were conducted at pH = 5.5.

We also assessed AD-L or S-AD-L (sorafenib-only) nanoparticles as the controls without hemin. Indeed, nor notable color absorbance neither fluorescence was observed when they were incubated with TMB or HPF in the presence of H_2O_2; whereas clear oxTMB absorbance peaks and bright green HPF fluorescence were detected when H-AD-L (hemin-only) or SH-AD-L nanoparticles were added (Figure 3C and S8A). Collectively, these results confirmed the generation of •OH and hemin functioning as the catalytic center, as no reaction occurred in the absence of hemin (Figure 3C and S8A). Moreover, almost no oxTMB absorbance or HPF fluorescence was observed after mixing SH-AD-L nanoparticles in the absence of H_2O_2 (Figure 3D and S8B). Finally, increasing the concentration of SH-AD-L nanoparticles enhanced the POD-mimic catalytic activity (Figure 3E and S8C). All these data demonstrate that SH-AD-L nanoparticles retain the properties of hemin to catalyze H_2O_2 to •OH.

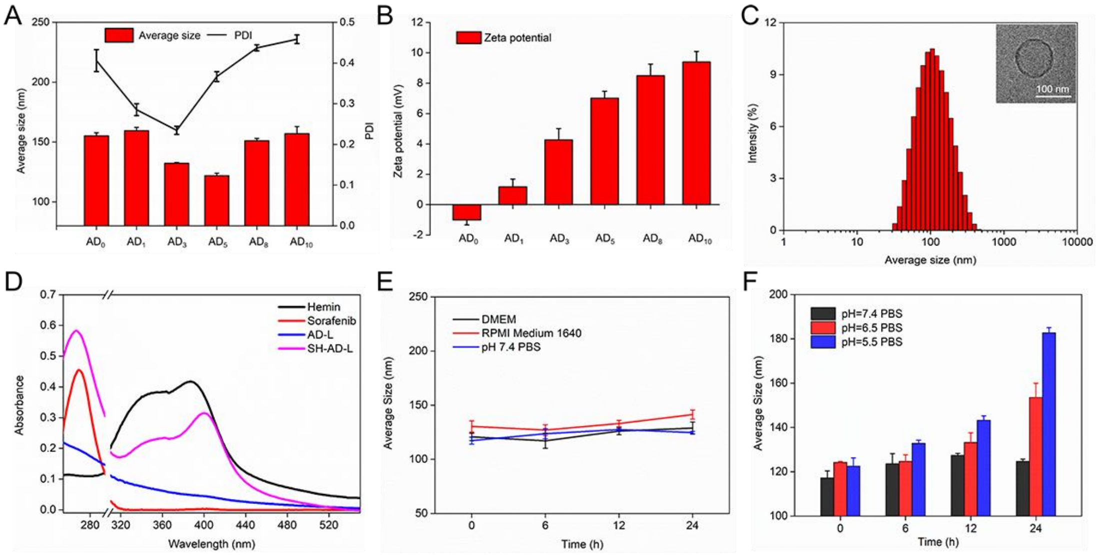

Figure 2. Characterizations of AD-L and SH-AD-L nanoparticles. (A) Average size and PDI value, (B) Zeta potential of AD_n-L vesicles with different molar ratios of AD. (C) Size distribution and cryo-TEM image of SH-AD-L nanoparticles. (D) UV-vis absorption spectra of hemin, sorafenib, and AD-L and SH-AD-L nanoparticles. (E) Stability of SH-AD-L in different media for 24h. (F) Stability of SH-AD-L in PBS solution at pH 7.4, pH 6.5, and pH 5.5 for 24h. Data are presented as mean ± S.D (n=3).

To further evaluate the catalytic efficiency of SH-AD-L nanoparticles, we carried out kinetic analysis using different concentrations of H_2O_2 at pH = 5.5 at room temperature. The absorbance of the reaction solution was monitored in real time at 650 nm for the formation of the reaction product (oxTMB) (Figure 3F), and the initial reaction rates (υ) were calculated according to the Beer–Lambert law (ε = 39,000 M^{-1} cm^{-1} for oxTMB) for the corresponding H_2O_2 concentration. The reaction rate was then plotted against the H_2O_2 concentration and fitted with a Michaelis–Menten curve (Figure 3G). Furthermore, a linear double-reciprocal plot (Lineweaver–Burk plot and Figure 3H) was used to get the Michaelis–Menten constant (K_m) and the maximum reaction rate (V_{max}). The K_m and V_{max} for SH-AD-L nanoparticles were calculated to be 13.7 mM and 7.48×10^{-8} M s^{-1} respectively (Figure 3H). Based on the K_m, which represents affinity for the substrate, the SH-AD-L nanoparticles displayed higher affinity than most reported nanozymes (Table S2).

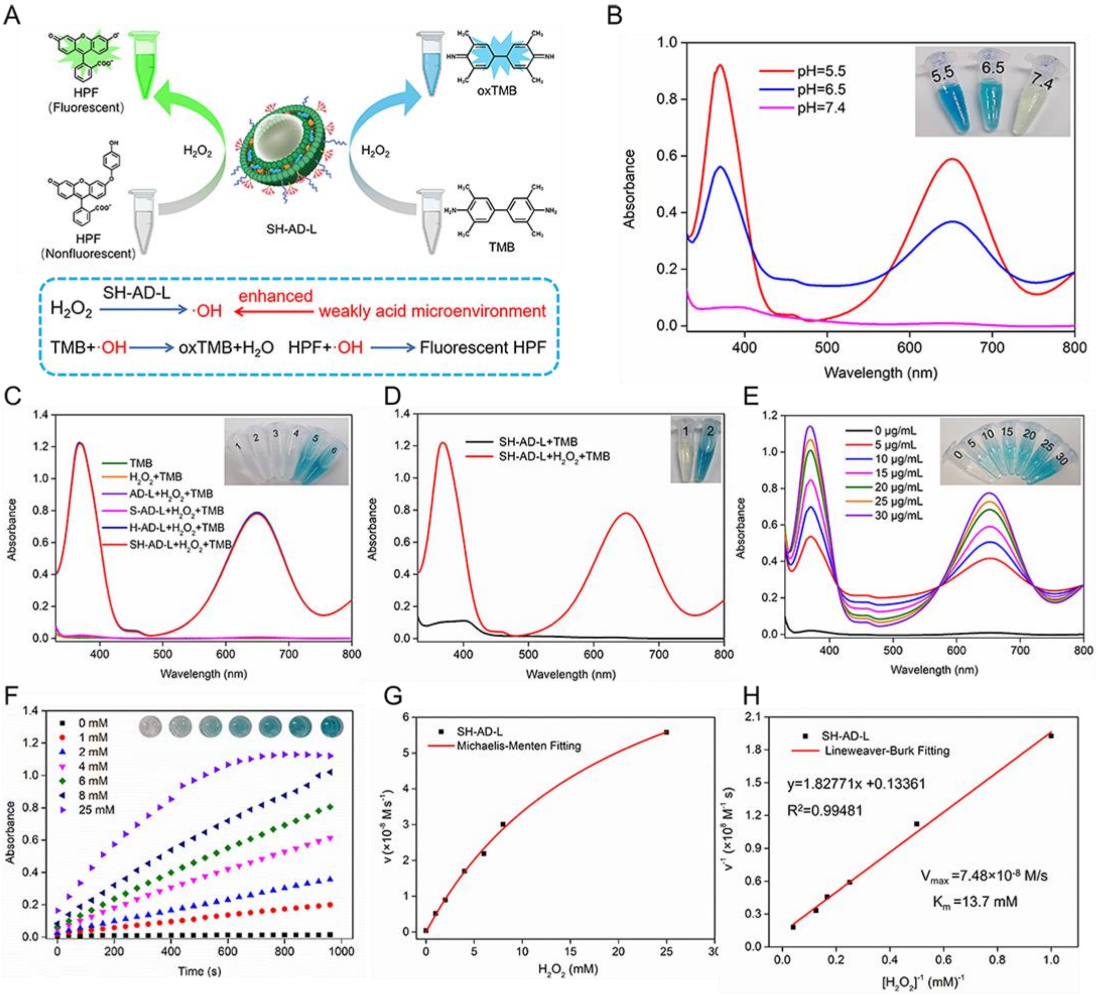

Figure 3. Characterization of the POD-mimic catalytic activity of SH-AD-L nanoparticles. (A) Schematic of the POD-mimic catalytic characteristics of SH-AD-L nanoparticles. (B) UV-vis absorption spectra of oxTMB in pH 5.5, 6.5, and 7.4 PBS. UV-vis absorption spectra of oxTMB oxidized by (C) different nanoparticles in the presence of H_2O_2, (D) SH-AD-L alone and SH-AD-L+H_2O_2, and (E) different concentrations of SH-AD-L with H_2O_2. (F) Time-dependent absorbance changes of oxTMB at 650 nm after the addition of various H_2O_2 concentrations (0, 1, 2, 4, 6, 8, and 25 mM). Inset: photograph of the corresponding sample solutions after 960 s. (G) Michaelis–Menten kinetic analysis and (H) Lineweaver–Burk plots for SH-AD-L nanoparticles with H_2O_2 as the substrate. The concentration of TMB was 1 mM and the H_2O_2 concentrations varied. The initial reaction rate was calculated in ten periods (40 s per period). Inset: photograph of the corresponding sample solutions.

To achieve effective anticancer activity, it is important that the drug delivery system can cross cell membrane and enter cell. We therefore examined cellular uptake of SH-AD-L nanoparticles using laser scanning confocal microscopy (LSCM). Briefly, the human HCC cell line SMMC7721 was treated with indocyanine green (ICG)–labeled SH-AD-L nanoparticles. LSCM images showed that the ICG-SH-AD-L nanoparticles were internalized effectively within SMMC7721 cells (Figure 4A). Importantly, significant ICG-SH-AD-L nanoparticles were located within the endosomes, as revealed using LysoTracker Red staining (Figure 4A).

The acidic environment within endosome is a beneficial feature to promote drug release and increase the POD-mimic activity of SH-AD-L nanoparticles.

We next assessed the cytotoxicity of SH-AD-L nanoparticles on SMMC7721 cells at various concentrations. As shown in Figure 4B, empty liposomal vesicles showed almost no toxicity at all, while SH-AD-L nanoparticles exhibited concentration-dependent cytotoxicity. Notably, SH-AD-L nanoparticles were more cytotoxic than H-AD-L or S-AD-L nanoparticles, likely because of the amplified oxidative stress caused by the simultaneous sorafenib-induced GSH depletion and hemin-triggered Fenton reaction. Also, an annexin V-fluorescein isothiocyanate/propidium iodide (PI) assay was performed to evaluate SH-AD-L-induced apoptosis (Figure 4C). H-AD-L nanoparticles induced little apoptosis, whereas both S-AD-L and SH-AD-L nanoparticles induced considerable apoptosis, with SH-AD-L nanoparticles achieving the highest level. This can be ascribed to the enhanced therapeutic sensitivity of sorafenib resulting from the production of •OH. The cytotoxicity of various liposomal vesicles was also assessed using calcein-AM/propidium iodide staining to visually observe the live/dead cells (Figure S9 and S10), which yielded results consistent with those obtained using MTS assay (Figure 4B). Meanwhile, we also explore the uptake behavior and the cytotoxicity of MIHA cells (normal liver cells) after treatment with SH-AD-L. The LSCM images suggested that the fluorescent signals in SMMC7721 cells are slightly brighter than that in MIHA cells after incubating with ICG-SH-AD-L for 0.5h and 4h (Figure S11A and S11B). The corresponding fluorescent intensity of ICG measured by flow cytometry was higher in SMMC7721 cells than in MIHA cells (Figure S11C and S11D). It is worth noting that SH-AD-L showed less cytotoxicity to MIHA cells compared to SMMC7721 cells (Figure S11E and 4B). This is mainly ascribed to the fact that the distinct environment in tumor cells with high levels of GSH and ROS, resulting in the combination treatment of sorafenib and hemin is more effective against tumor cells.

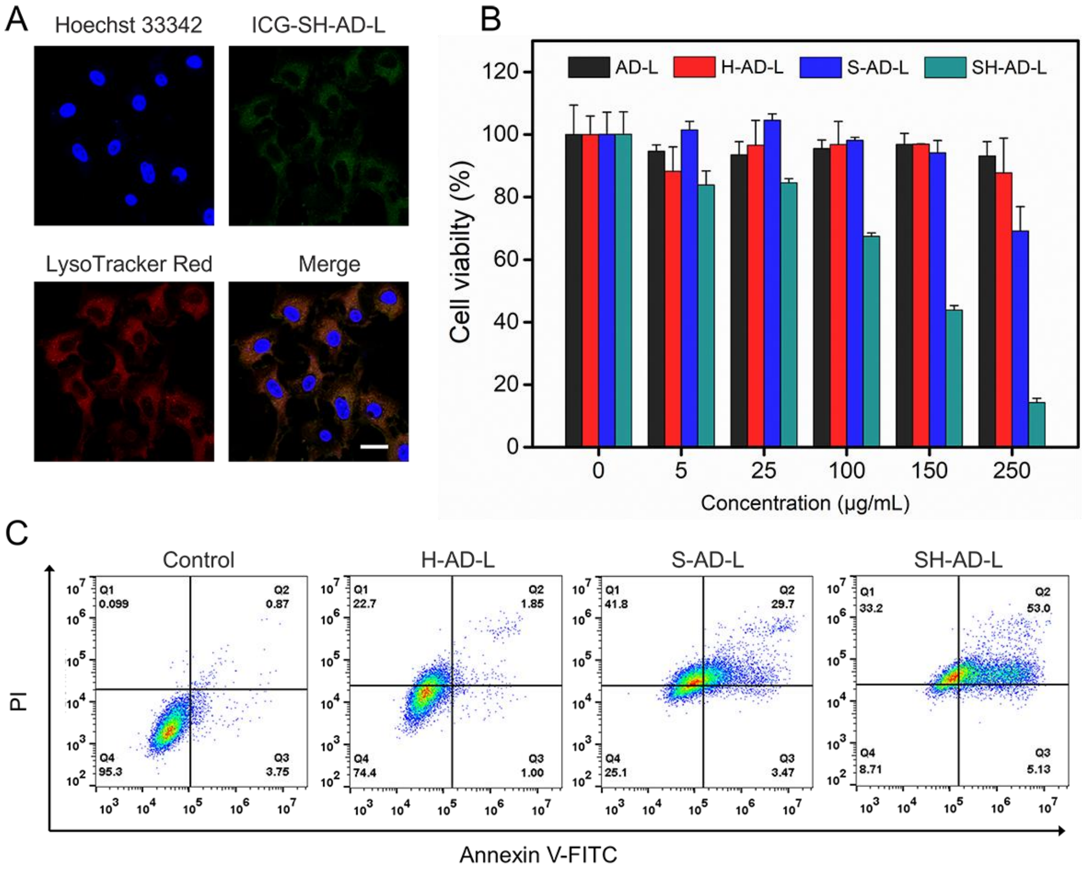

Figure 4. (A) Cellular uptake of SH-AD-L nanoparticles by SMMC7721 cells after incubation for 4 h. SH-AD-L nanoparticles were labeled with ICG, nuclei were stained with Hoechst 33342, and endosomes were stained with LysoTracker Red DND-99. Scale bar = 20 μm. (B) *In vitro* cell viability of SMMC7721 cells after treatment with AD-L, H-AD-L, S-AD-L, and SH-AD-L nanoparticles for 24 h. Data are presented as mean ± S.D (n=5). (C) Flow cytometry analysis of apoptotic SMMC7721 cells induced by various treatments.

Based on the effective cancer cell killing capacity of SH-AD-L nanoparticles, we further verified whether the anticancer effect indeed occurred by inducing ferroptosis in tumor cells via GSH depletion, Fe^{2+} overload, and •OH production (Figure 5A). Rapid GSH depletion can inhibit the activity of GPX4 and result in inability to reduce the toxic LPO to nontoxic lipid alcohols. We therefore first quantified GSH levels in SMMC7721 cells. Remarkably, a significant decrease in GSH content was observed in cells treated with SH-AD-L compared to those with H-AD-L and S-AD-L nanoparticles (Figure 5B). Also, the expression of GPX4 decreased following treatment with SH-AD-L nanoparticles, as revealed by immunofluorescence (Figure 5C).

Since activating HMOX-1 can degrade heme into Fe^{2+} [17], thereby increasing the iron pool for potential ferroptosis, we then examined the HMOX-1 protein expression using LSCM. Notably, both H-AD-L and SH-AD-L nanoparticles upregulated the expression of HMOX-1 protein, indicating that hemin is indeed involved in and responsible for HMOX-1 upregulation (Figure 5D). We also assessed the intracellular Fe^{2+} levels using the fluorescent dye FeRhoNOX-1 as the Fe^{2+} indicator. Effectively, the fluorescence intensity of FeRhoNOX-1 was markedly increased following treatment with SH-AD-L nanoparticles, as demonstrated by both

LSCM images and flow cytometry analysis (Figure 5E and F). These results highlight that hemin released from SH-AD-L nanoparticles plays a role in activating the HMOX-1 protein, resulting in Fe^{2+} overloading. It is worth noting that both the hemin from the SH-AD-L nanoparticles and the increased concentration of Fe^{2+} can react with H_2O_2 to generate •OH, which can elevate intracellular reactive oxygen species (ROS) levels, accelerate LPO generation, and eventually induce ferroptosis. As shown in Figure 5G, •OH production was indeed observed, as revealed using LSCM images showing that tumor cells treated with SH-AD-L nanoparticles displayed the highest green fluorescence intensity. This was also supported by results obtained using flow cytometry analysis (Figure 5H).

The mechanism of antitumor ferroptosis was further studied using several typical ferroptosis inhibitors. In general, tumor cells express elevated levels of GSH to balance the high levels of ROS in tumor tissues and maintain redox homeostasis [27]. As expected, supplementation of the SH-AD-L nanoparticle with GSH and N-acetyl-l-cysteine (NAC, a precursor of GSH biosynthesis) resulted in enhanced cell protection (Figure 6A and B); this result demonstrates the GSH depletion activity of SH-AD-L nanoparticles in tumor cells. As shown in Figure 6C and D, treatment with Fer-1 (a ferroptosis inhibitor) and DFO (an iron-chelating agent) also alleviated the cytotoxicity induced by SH-AD-L nanoparticles, supporting for ferroptosis.

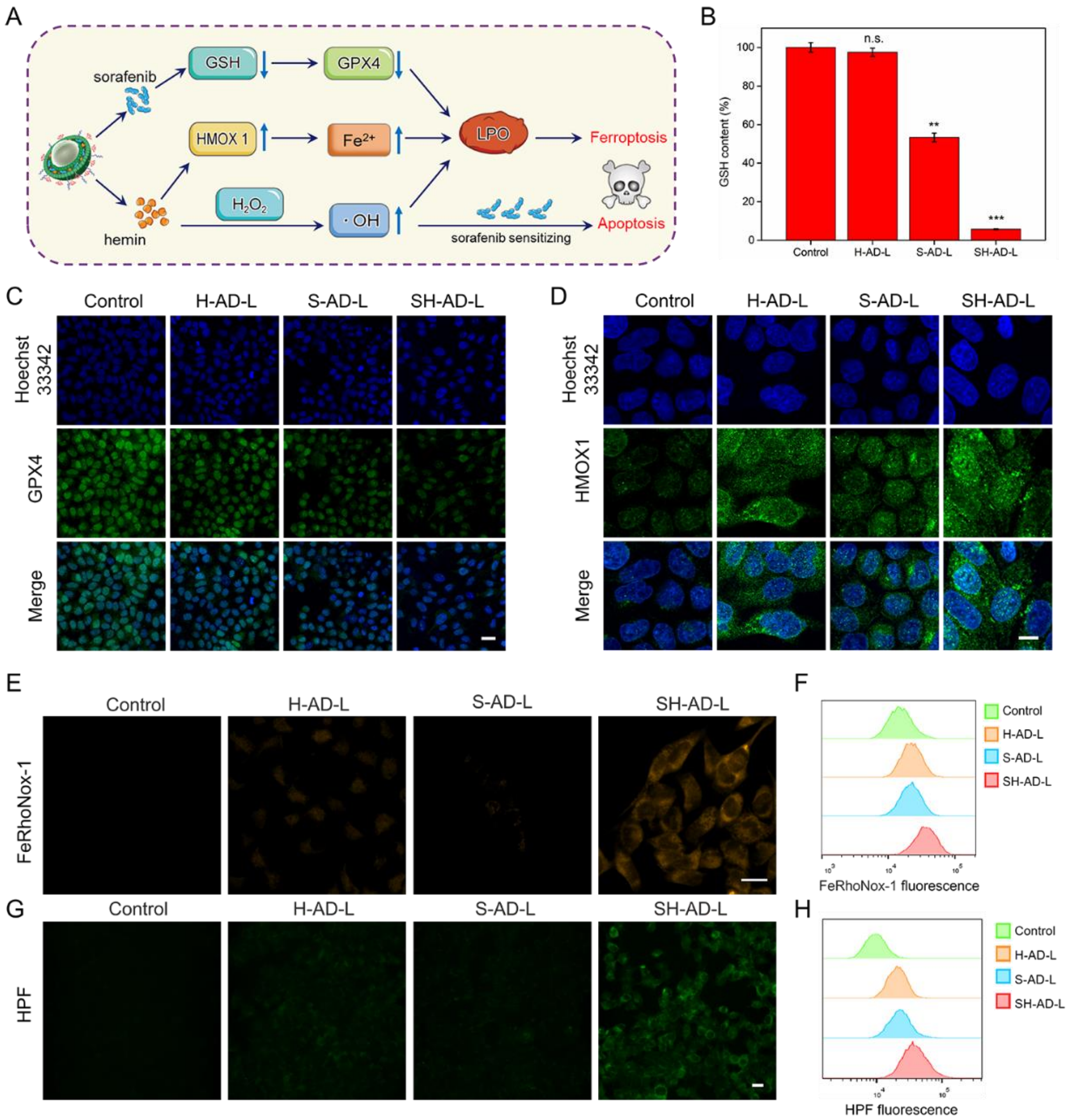

Figure 5. (A) Schematic of the mechanism of SH-AD-L nanoparticle-mediated ferroptosis-apoptosis in SMMC7721 cells. (B) GSH content in SMMC7721 cells after incubation with H-AD-L, S-AD-L, and SH-AD-L nanoparticles. Data are presented as mean ± S.D (n=3). Statistical analysis was analyzed using the Student's t-test. n.s., not significant, $^{**}p < 0.01$, and $^{***}p < 0.001$ of (B) compared with the control group. Immunofluorescence staining of (C) GPX4 (scale bar = 25 μm) and (D) HMOX-1 protein (scale bar = 10 μm) with different treatments, detected using LSCM. e-f) Intracellular Fe^{2+} levels evaluated by (E) LSCM (scale bar = 20 μm) and (F) flow cytometry after treatment with different nanoparticles. g-h) The generation of intracellular •OH analyzed by (G) LSCM (scale bar = 20 μm) and (H) flow cytometry after various treatments using HPF as the •OH probe.

Next, to investigate intracellular oxidative stress upon nanoparticle treatment, we used a ROS indicator, dichlorofluorescein diacetate (DCFH-DA), to evaluate intracellular ROS levels using LSCM (Figure S12). As expected, compared with H-AD-L and S-AD-L nanoparticles, a robust increase in ROS concentration was detected following treatment with SH-AD-L nanoparticles. This result highlights that SH-AD-L nanoparticles effectively reacted with excess H_2O_2 to produce toxic •OH and simultaneously disabled the antioxidant system by suppressing GSH biosynthesis in tumor cells, thereby boosting ROS accumulation and amplifying oxidative stress. ROS are considered to be important effectors of both ferroptosis and apoptosis, both of which are accompanied by mitochondrial dysfunction due to the accumulation of intracellular ROS. We therefore used the JC-1 probe to measure the mitochondrial membrane potential of SMMC7721 cells after various treatments. According to the LSCM images in Figure S13, cells treated with SH-AD-L showed the strongest green signals, which evidently indicated the decrease of mitochondrial membrane potential. Additionally, the morphology of SMMC7721 cells treated with SH-AD-L observed using bio-TEM showed shrunken mitochondria, increased membrane intensity, and the decreased or loss of mitochondrial ridges compared to the control groups (Figure S14), which are regarded as the typical characteristics of ferroptosis. To further demonstrate the occurrence of ferroptosis after treatment, we used the lipophilic fluorescent probe BODIPY-C11 and the malondialdehyde (MDA) assay kit to evaluate the level of lipid peroxidation. As shown in Figure 6E, LPO were observed upon treatment with SH-AD-L nanoparticles, but not with H-AD-L or S-AD-L nanoparticles; these results were in line with those obtained using flow cytometry (Figure 6F). MDA, another typical biomarker, and end-product of lipid peroxidation during ferroptosis, was also obviously elevated in SH-AD-L treatment group (Figure S15). The accumulation of LPO can be ascribed to the amplification of oxidative stress caused by intracellular Fe^{2+} overloading and •OH production. In addition, GPX4 inactivation caused by GSH depletion failed to reduce toxic LPO to nontoxic lipid alcohols and enhance the accumulation of lipid ROS, as shown in Figure 5C and 5D. Taken together, our results provide evidence that SH-AD-L nanoparticles amplify oxidative stress-induced cell damage and enhance the synergistic therapeutic effects of ferroptosis and apoptosis.

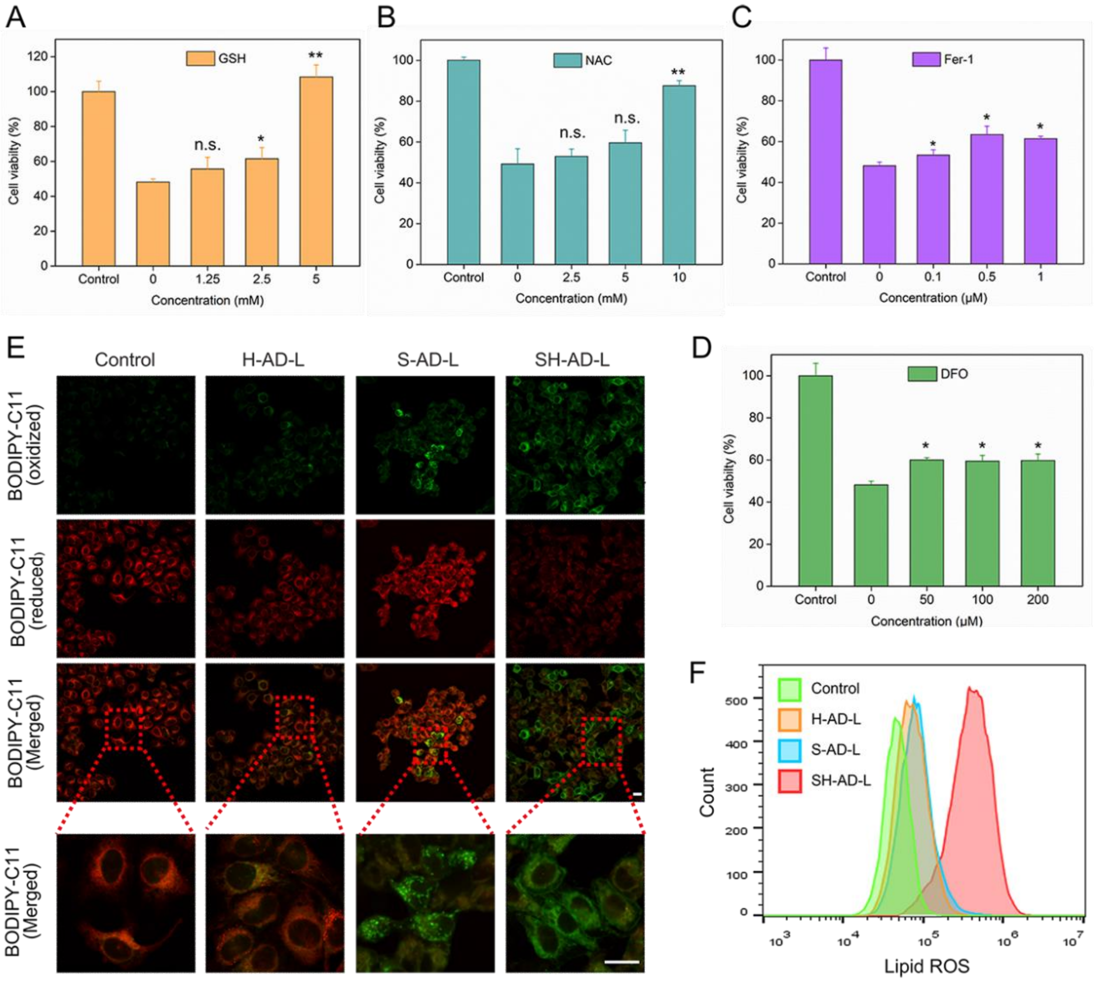

Figure 6. Cell viability of SMMC7721 cells treated with SH-AD-L nanoparticles in combination with (A) GSH, (B) NAC, (C) Fer-1, and (D) DFO. GSH, glutathione; NAC, N-acetyl-l-cysteine; Fer-1, ferrostatin-1; DFO, deferoxamine mesylate. Data are presented as mean ± S.D (n=3). Statistical analysis was analyzed using the Student's t-test. n.s., not significant, $^*p < 0.05$, and $^{**}p < 0.01$ of (A-D) compared with SH-AD-L treated groups without ferroptosis inhibitors addition. Lipid peroxidation in SMMC7721 cells was analyzed by (E) LSCM (scale bar = 20 μm) and (F) flow cytometry after treatment with different nanoparticles for 24 h, using fluorescent BODIPY-C11 as a probe for lipid peroxidation.

To assess the antitumor effects of SH-AD-L nanoparticles *in vivo*, we established tumor-xenograft nude mice using SMMC7721. When the tumor volume grew to approximately 100 mm^3, the tumor-bearing mice were randomly divided into four groups and intravenously administered PBS, H-AD-L nanoparticles, S-AD-L nanoparticles, and SH-AD-L nanoparticles, respectively (Figure 7A). Compared with the control group, the H-AD-L and S-AD-L nanoparticle groups exhibited moderate inhibition on tumor growth, whereas the SH-AD-L nanoparticle group showed the best tumor suppression, further supporting the synergistic effect of hemin and sorafenib (Figure 7B). Quantification of the weights of the dissected tumors at the end of treatment yielded results consistent with those of tumor growth inhibition (Figure 7C and S16). In addition, we did not observe any noticeable changes in body weight in any treatment group (Figure 7D), nor illness, indicating good biocompatibility of the AD-doped the liposomal vesicles.

We also performed histopathological analysis of tumor tissue to further evaluate therapeutic efficacy. As shown in Figure 7E, hematoxylin and eosin (H&E) staining revealed severe cell damage in the SH-AD-L nanoparticle group compared with the other groups. Terminal deoxynucleotidyl transferase dUTP nick-end labeling (TUNEL) staining and immunohistochemical staining for Ki67 revealed increased apoptosis and decreased cell proliferation rates following SH-AD-L nanoparticle treatment. Also, immunofluorescence staining demonstrated reduced expression of GPX4 and increased expression of HMOX-1 in the tumors of SH-AD-L nanoparticle-treated mice (Figure S17), indicating the occurrence of ferroptosis which is in line with the *in vitro* results. Furthermore, H&E staining of the major organs (heart, liver, spleen, lung, and kidney) demonstrated no notable toxicity associated with SH-AD-L nanoparticle treatment (Figure S18). Taken together, treatment with SH-AD-L nanoparticles demonstrated significant ferroptosis-apoptosis antitumor activity without obvious side effects *in vivo*.

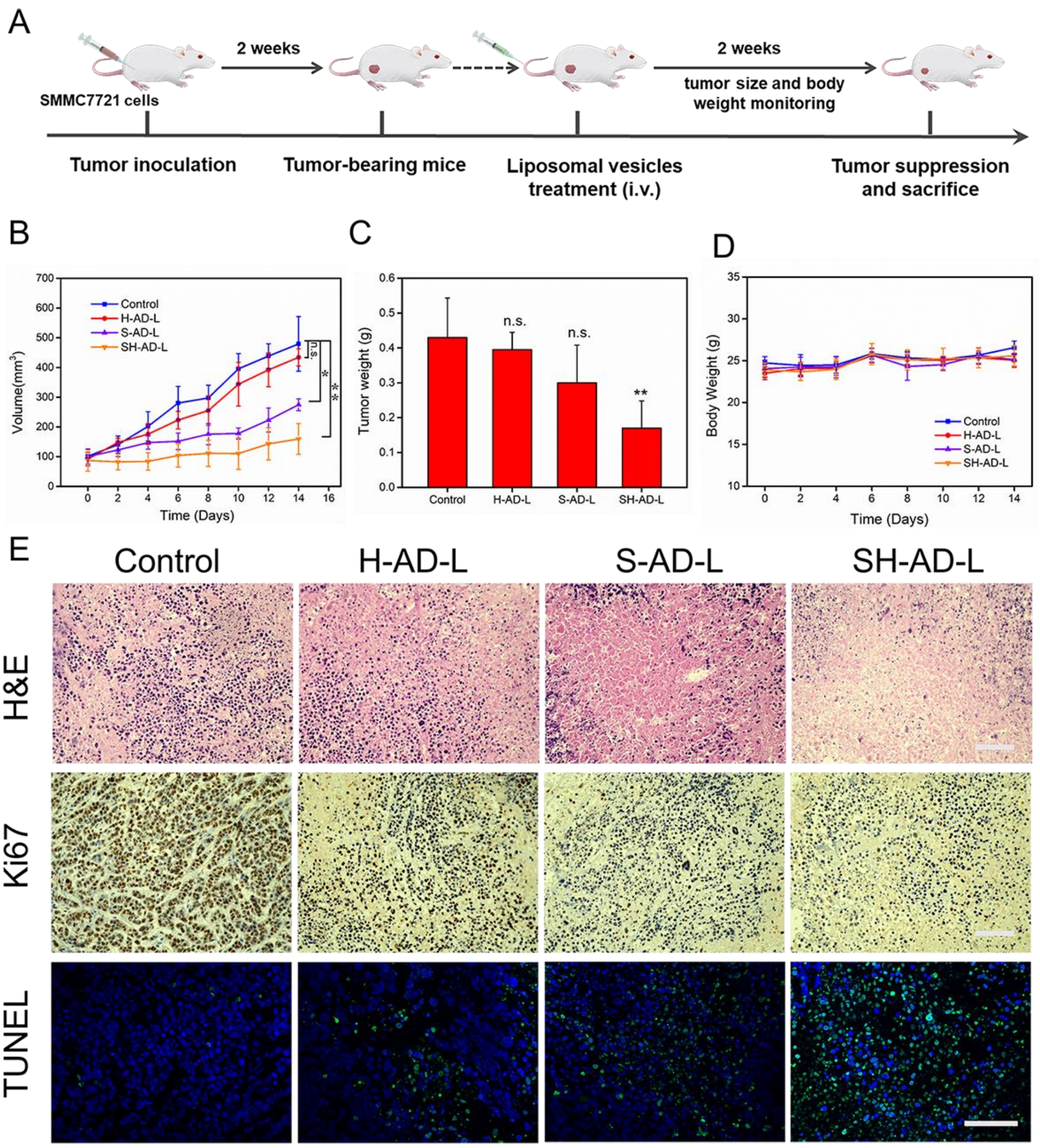

Figure 7. Antitumor therapy with SH-AD-L nanoparticles. (A) Schematic of the generation of SMMC7721-xenografted nude mice and treatment procedures. (B) Changes in tumor volume during the treatment period. Data are presented as mean ± S.D (n=3). Statistical analysis was analyzed using the Student's t-test. n.s., not significant, $*p < 0.05$, and $**p < 0.01$ of (B-C) compared with the control group. (C) Tumor weight at the end of the treatment. (D) Changes in mouse body weight during the treatment period. (E) H&E staining, Ki67 immunohistochemistry, and TUNEL staining of tumor sections following the different treatments (scale bar = 100 μm).

Conclusion

In summary, we have presented an innovative type of pH-responsive hybrid liposomal vesicle system, SH-AD-L nanoparticles, for effective co-delivery of ferroptosis inducer (sorafenib) and iron catalyst (hemin) for synergistic ferroptosis-apoptosis to treat advanced HCC. We found that doping of amine-terminated amphiphilic dendrimers markedly enhanced the pH sensitivity of traditional liposomes, which was particularly favorable for efficient drug delivery in weakly acidic tumor microenvironment. The release of sorafenib in tumors blocked GSH biosynthesis and downregulated GPX4 expression, thereby impairing the antioxidant function of the GPX4-GSH-cysteine axis. Meanwhile, hemin provided POD-mimic catalytic activity and upregulated HMOX-1 to promote Fe^{2+} overload, which was accompanied by highly toxic •OH overproduction, contributing to tumor suppression. All these act in a coordinated manner to induce LPO accumulation and ferroptotic damage, and the high concentration of •OH enhanced the sorafenib-mediated cell apoptosis. Consequently, SH-AD-L nanoparticle treatment achieved successful tumor suppression *in vivo*. These encouraging results indicate that hemin is a promising candidate to synergize with sorafenib for advanced HCC therapy. It is also important to note that the designed pH-responsive hybrid liposomal vesicles based on AD-doped liposome hold promise for safe and efficient drug delivery in tumor therapy, which is anticipated to find broad applications in nanomedicine.

Experimental Section

Preparation of Hybrid Liposomal Vesicle and SH-AD-L Nanoparticle: The liposomal vesicles are formed in aqueous phase by self-assembling of the amphipathic phospholipid molecules into bilayer structure, in which the lipid chains face each other to form a hydrophobic area, while the hydrophilic head groups are aligned toward the aqueous phase [28]. Herein, we used thin-film hydration, the most common method for liposome preparation. In this method, lipids, amphiphilic molecules, and hydrophobic drugs are dissolved and mixed in the organic solvent. The organic solvent is removed using a rotary evaporator under vacuum, forming a thin film in the bottom of the round-bottom flask, and the film is subsequently hydrated in water or buffer solution to form vesicles [29]. The main steps of our study are as follows: the ingredients (AD: DPPC: cholesterol: $DSPE\text{-}PEG_{2000}$= n: 41.7: 8.3: 2.9, mol: mol) were dissolved in a mixed solvent (trichloromethane: methanol=3:1, v/v), and the organic solvent was removed to form a lipid film under vacuum rotary evaporation (100 rpm, 37°C). Afterward, the film was hydrated by adding the preheated PBS solution at 37°C and sonicated for 3 min in an ice bath to obtain the hybrid liposomal vesicles. During the preparation process the digital letter n=0, 1, 3, 5, 8,10, while the molar ratios of DPPC, cholesterol, and $DSPE\text{-}PEG_{2000}$ were kept constant. For drug loading, sorafenib and hemin were also dissolved in the mixed solvent and mixed with the lipid solution to form a film under the same condition, and the obtained product was filtered through a 0.22-μm membrane to remove the unencapsulated sorafenib and hemin. ICG was used for the preparation of ICG-labeled SH-AD-L nanoparticles by following the above process. AD-L, S-AD-L, and H-AD-L were also prepared by following the above process without introducing the corresponding ingredients

Animal Model: Male BALB/c nude mice (five weeks old) were used to establish the SMMC7721 tumor-bearing mice. All animal experiments were performed in accordance with the protocol approved by the Institutional Animal Care and Use Committee of University of Macau (approval number: UMARE-013-2022). SMMC7721 cells suspended in PBS/Matrigel matrix were injected into the right flank. The xenograft tumor model of advanced liver cancer was established according to the previous literature [30]. The tumor volume would reach about 100 mm^3 after 2 weeks, the tumor-bearing mice will be used for *in vivo* antitumor studies.

In Vivo Anticancer Effect of SH-AD-L Nanoparticles: To study the antitumor effect, SMMC7721 tumor-bearing mice were randomly divided into four groups and intravenously administrated with PBS, H-AD-L, S-AD-L, and SH-AD-L (10 mg/kg sorafenib, 2.67 mg/kg hemin) every two days. The tumor volumes and body weight of mice were also recorded every two days. The tumor volumes were calculated according to the equation: $\text{volume}=\text{length}\times\text{width}^2/2$. After treatment, all of the tumor-bearing mice were sacrificed, digital photos of the tumors were captured, and the weight of every tumor was recorded. Subsequently, major organs (hearts, livers, spleens, lungs, and kidneys) were collected and fixed in 4% paraformaldehyde to perform H&E staining to assess the biosafety of SH-AD-L. In addition, the tumor tissues were used for TUNEL staining, Ki67 immunohistochemical staining, and HMOX1 and GPX4 immunofluorescence staining to further evaluate the therapeutic effects and the expression levels of HMOX1 and GPX4 after treatment. The stained tumor sections were observed and captured by an optical microscope and LSCM.

Statistical Analysis: All the experimental data are presented as the mean ± standard deviation ($n\geq3$). The significant difference was analyzed by an unpaired two-tailed Student's t-test. n.s., not significant, $^*p < 0.05$, $^{**}p < 0.01$, and $^{***}p < 0.001$ (* represents statistical significance). IBM SPSS Statistics 20 software was used for statistical analysis.

Acknowledgements

This work was funded by the Science and Technology Development Fund, Macau SAR (File No. 0085/2020/A2, 0114/2019/A2, FDCT 0016/2020/A1), the Guangdong Provincial Key Laboratory of Tumor Interventional Diagnosis and Treatment (2021B1212040004), the Natural Science Foundation of Guangdong Province of China (2022B1515020010), the Research Grant of University of Macau (Grant No.: MYRG2020-00130-FHS, MYRG2022-00036-FHS, MYRG 2022-00240-FHS), the National Natural Science Foundation of China (Grant No. 62027901), the Foundation of Department of Science and Technology of Sichuan Province (2020YFQ0004), and La Ligue contre Le Cancer (EL2016, EL2021 LNCCLiP). We also thank the core facilities at the Faculty of Health Sciences, especially the drug development core, bioimaging, stem cell core and animal facility for their excellent services.

Keywords: amphiphilic dendrimer • liposomal vesicle • ferroptosis • synergistic therapy • advanced hepatocellular carcinoma

References

[1] B. A. Carneiro, W. S. El-Deiry, *Nat. Rev. Clin. Oncol.* **2020**, *17*, 395-417.

[2] a) L. Gao, Z. X. Wu, Y. G. Assaraf, Z. S. Chen, L. Wang, *Drug Resist. Updat.* **2021**, *57*, 100770; b) A. Valente, A. Podolski-Renic, I. Poetsch, N. Filipovic, O. Lopez, I. Turel, P. Heffeter, *Drug Resist. Updat.* **2021**, *58*.

[3] a) G. Lei, C. Mao, Y. Yan, L. Zhuang, B. Gan, *Protein Cell* **2021**, *12*, 836-857; b) X. Chen, J. Li, R. Kang, D. J. Klionsky, D. Tang, *Autophagy* **2021**, *17*, 2054-2081.

[4] a) C. Zhang, X. Liu, S. Jin, Y. Chen, R. Guo, *Mol. Cancer* **2022**, *21*, 47; b) Q. Zeng, X. Ma, Y. Song, Q. Chen, Q. Jiao, L. Zhou, *Theranostics* **2022**, *12*, 817-841.

[5] a) L. Zhou, W. Feng, L. Chen, H. Huang, S. Huang, Q. Chen, X. Zhang, Y. Chen, *Nano Today* **2022**, *46*, 101623; b) L. Liang, L. Wen, Y. Weng, J. Song, H. Li, Y. Zhang, X. He, W. Zhao, M. Zhan, Y. Li, L. Lu, Y. Xin, C. Lu, *Chem. Eng. J.* **2021**, *425*, 131451.

[6] a) P. Koppula, L. Zhuang, B. Gan, *Protein & Cell* **2020**, *12*, 599-620; b) B. Gan, *Signal Transduct. Target. Ther.* **2022**, *7*, 128; c) L. Zhou, W. Feng, Y. Mao, Y. Chen, X. Zhang, *Bioact. Mater.* **2023**, 24, 26-36.

[7] H. Sung, J. Ferlay, R. L. Siegel, M. Laversanne, I. Soerjomataram, A. Jemal, F. Bray, *CA Cancer J. Clin.* **2021**, *71*, 209-249.

[8] a) S. K. Qin, F. Bi, S. Z. Gu, Y. X. Bai, Z. D. Chen, Z. S. Wang, J. E. Ying, Y. Y. Lu, Z. Q. Meng, H. M. Pan, P. Yang, H. L. Zhang, X. Chen, A. B. Xu, C. X. Cui, B. Zhu, J. Wu, X. L. Xin, J. F. Wang, J. L. Shan, J. H. Chen, Z. D. Zheng, L. Xu, X. Y. Wen, Z. Y. You, Z. G. Ren, X. F. Liu, M. Qiu, L. Q. Wu, F. Chen, *J. Clin. Oncol.* **2021**, *39*, 3002-3011; b) T. Yau, J.-W. Park, R. S. Finn, A.-L. Cheng, P. Mathurin, J. Edeline, M. Kudo, J. J. Harding, P. Merle, O. Rosmorduc, L. Wyrwicz, E. Schott, S. P. Choo, R. K. Kelley, W. Sieghart, E. Assenat, R. Zaucha, J. Furuse, G. K. Abou-Alfa, A. B. El-Khoueiry, I. Melero, D. Begic, G. Chen, J. Neely, T. Wisniewski, M. Tschaika, B. Sangro, *Lancet Oncol.* **2022**, *23*, 77-90.

[9] a) J. Chen, X. Li, C. Ge, J. Min, F. Wang, *Cell Death Differ.* **2022**, 29, 467-480; b) X. Hu, Y. He, Z. Han, W. Liu, D. Liu, X. Zhang, L. Chen, L. Qi, L. Chen, Y. Luo, Q. Li, P. Chen, Q. Wu, X. Zhu, H. Guo, *Cell Death Dis*. **2022**, 13, 1010.

[10] J. M. Llovet, S. Ricci, V. Mazzaferro, P. Hilgard, E. Gane, J. F. Blanc, A. C. de Oliveira, A. Santoro, J. L. Raoul, A. Forner, M. Schwartz, C. Porta, S. Zeuzem, L. Bolondi, T. F. Greten, P. R. Galle, J. F. Seitz, I. Borbath, D. Häussinger, T. Giannaris, M. Shan, M. Moscovici, D. Voliotis, J. Bruix, *N. Engl. J. Med.* **2008**, *359*, 378-390.

[11] a) J. Feng, P. Z. Lu, G. Z. Zhu, S. C. Hooi, Y. Wu, X. W. Huang, H. Q. Dai, P. H. Chen, Z. J. Li, W. J. Su, C. Y. Han, X. P. Ye, T. Peng, J. Zhou, G. D. Lu, *Acta Pharmacol. Sin.* **2021**, *42*, 160-170; b) L. Zhong, Y. Li, L. Xiong, W. Wang, M. Wu, T. Yuan, W. Yang, C. Tian, Z. Miao, T. Wang, S. Yang, *Signal Transduct. Target. Ther.* **2021**, *6*, 201.

[12] a) A. Ajoolabady, D. Tang, G. Kroemer, J. Ren, *Br. J. Cancer* **2022**, doi: 10.1038/s41416-022-01998-x; b) Z. J. Li, H. Q. Dai, X. W. Huang, J. Feng, J. H. Deng, Z. X. Wang, X. M. Yang, Y. J. Liu, Y. Wu, P. H. Chen, H. Shi, J. G. Wang, J. Zhou, G. D. Lu, *Acta Pharmacol. Sin*. **2021**, 42, 301-310.

[13] C. Louandre, Z. Ezzoukhry, C. Godin, J. C. Barbare, J. C. Maziere, B. Chauffert, A. Galmiche, *Int. J. Cancer* **2013**, *133*, 1732-1742.

[14] a) X. Sun, X. Niu, R. Chen, W. He, D. Chen, R. Kang, D. Tang, *Hepatology* **2016**, 64, 488-500; b) X. Sun, Z. Ou, R. Chen, X. Niu, D. Chen, R. Kang, D. Tang, *Hepatology* **2016**, 63, 173-184.

[15] J. Sun, C. Zhou, Y. Zhao, X. Zhang, W. Chen, Q. Zhou, B. Hu, D. Gao, L. Raatz, Z. Wang, P. J. Nelson, Y. Jiang, N. Ren, C. J. Bruns, H. Zhou, *Redox Biol.* **2021**, 41, 101942.

[16] J. Chen, F. Chen, L. Zhang, Z. Yang, T. Deng, Y. Zhao, T. Zheng, X. Gan, H. Zhong, Y. Geng, X. Fu, Y. Wang, C. Yu, *ACS Appl. Mater. Interfaces* **2021**, *13*, 27856-27867.

[17] a) B. Hassannia, B. Wiernicki, I. Ingold, F. Qu, S. Van Herck, Y. Y. Tyurina, H. Bayır, B. A. Abhari, J. P. F. Angeli, S. M. Choi, E. Meul, K. Heyninck, K. Declerck, C. S. Chirumamilla, M. Lahtela-Kakkonen, G. Van Camp, D. V. Krysko, P. G. Ekert, S. Fulda, B. G. De Geest, M. Conrad, V. E. Kagan, W. Vanden Berghe, P. Vandenabeele, T. Vanden Berghe, *J. Clin. Invest.* **2018**, *128*, 3341-3355; b) X. Fang, H. Wang, D. Han, E. Xie, X. Yang, J. Wei, S. Gu, F. Gao, N. Zhu, X. Yin, Q. Cheng, P. Zhang, W. Dai, J. Chen, F. Yang, H. T. Yang, A. Linkermann, W. Gu, J. Min, F. Wang, *Proc. Natl. Acad. Sci. U. S. A.* **2019**, *116*, 2672-2680.

[18] a) S. K. NaveenKumar, B. N. SharathBabu, M. Hemshekhar, K. Kemparaju, K. S. Girish, G. Mugesh, *ACS Chem. Biol.* **2018**, *13*, 1996-2002; b) B. Hassannia, P. Vandenabeele, T. Vanden Berghe, *Cancer cell* **2019**, *35*, 830-849; c) K. Li, K. Xu, Y. He, L. Lu, Y. Mao, P. Gao, G. Liu, J. Wu, Y. Zhang, Y. Xiang, Z. Luo, K. Cai, *Small* **2021**, *17*, e2102046.

[19] a) T. Liu, W. Liu, M. Zhang, W. Yu, F. Gao, C. Li, S. B. Wang, J. Feng, X. Z. Zhang, *ACS Nano* **2018**, *12*, 12181-12192; b) Z.-H. Li, Y. Chen, X. Zeng, X.-Z. Zhang, *Nano Today* **2021**, *38*, 101150.

[20] H. Li, M. Huang, Z. Wei, J. He, Y. Ma, C. Lu, A. Jin, Z. Wang, L. Wen, *Front. Bioeng. Biotechnol.* **2022**, *10*, 1032571.

[21] Y. Zheng, X. Li, C. Dong, L. Ding, H. Huang, T. Zhang, Y. Chen, R. Wu, *Adv. Funct. Mater.***2021**, *32*, 2107529.

[22] a) X. X. Liu, J. H. Zhou, T. Z. Yu, C. Chen, Q. Cheng, K. Sengupta, Y. Y. Huang, H. T. Li, C. Liu, Y. Wang, P. Posocco, M. H. Wang, Q. Cui, S. Giorgio, M. Fermeglia, F. Q. Qu, S. Pricl, Y. H. Shi, Z. C. Liang, P. Rocchi, J. J. Rossi, L. Peng, *Angew. Chem. Int. Ed. Engl.* **2014**, *53*, 11822-11827; b) S. S. Hinman, C. J. Ruiz, Y. Cao, M. C. Ma, J. Tang, E. Laurini, P. Posocco, S. Giorgio, S. Pricl, L. Peng, Q. Cheng, *ACS Appl. Mater. Interfaces* **2017**, *9*, 1029-1035; c) T. Wei, C. Chen, J. Liu, C. Liu, P. Posocco, X. Liu, Q. Cheng, S. Huo, Z. Liang, M. Fermeglia, S. Pricl, X. J. Liang, P. Rocchi, L. Peng, *Proc. Natl. Acad. Sci. U. S. A.* **2015**, *112*, 2978-2983.

[23] a) T. Yu, X. Liu, A. L. Bolcato-Bellemin, Y. Wang, C. Liu, P. Erbacher, F. Qu, P. Rocchi, J. P. Behr, L. Peng, *Angew. Chem. Int. Ed. Engl.* **2012**, *51*, 8478-8484; b) D. Dhumal, W. Lan, L. Ding, Y. Jiang, Z. Lyu, E. Laurini, D. Marson, A. Tintaru, N. Dusetti, S. Giorgio, J. L. Iovanna, S. Pricl, L. Peng, *Nano Res.* **2020**, *14*, 2247-2254; c) J. Liu, C. Chen, T. Wei, O. Gayet, C. Loncle, L. Borge, N. Dusetti, X. Ma, D. Marson, E. Laurini, S. Pricl, Z. Gu, J. Iovanna, L. Peng, X. J. Liang, *Exploration* **2021**, *1*, 21-34.

[24] a) S. Xu, S. Ling, Q. Shan, Q. Ye, Q. Zhan, G. Jiang, J. Zhuo, B. Pan, X. Wen, T. Feng, H. Lu, X. Wei, H. Xie, S. Zheng, J. Xiang, Y. Shen, X. Xu, *Adv. Sci.* **2021**, *8*, 2003042; b) T. C. Chou, *Cancer Res.* **2010**, *70*, 440-446.

[25] J. Chen, A. Ellert-Miklaszewska, S. Garofalo, A. K. Dey, J. Tang, Y. Jiang, F. Clement, P. N. Marche, X. Liu, B. Kaminska, A. Santoni, C. Limatola, J. J. Rossi, J. Zhou, L. Peng, *Nat. Protoc.* **2021**, *16*, 327-351.
[26] S. Gao, H. Lin, H. Zhang, H. Yao, Y. Chen, J. Shi, *Adv. Sci.* **2019**, *6*, 1801733.
[27] F. Wu, Y. Du, J. Yang, B. Shao, Z. Mi, Y. Yao, Y. Cui, F. He, Y. Zhang, P. Yang, *ACS Nano* **2022**, *16*, 3647-3663.
[28] K. Ajeeshkumar, P. A. Aneesh, N. Raju, M. Suseela, C. N. Ravishankar, S. Benjakul, *Compr. Rev. Food Sci. Food Saf.* **2021**, 20, 1280-1306.
[29] D. E. Large, R. G. Abdelmessih, E. A. Fink, D. T. Auguste, *Adv. Drug Deliv. Rev.* **2021**, 176, 113851.
[30] M. Yang, Y. Su, Z. Wang, D. Du, S. Wei, Z. Liao, Q. Zhang, L. Zhao, X. Zhang, L. Han, J. Jiang, M. Zhan, L. Sun, S. Yuan, Z. Zhou, *Biochem. Pharmacol.* **2021**, *190*, 114641.

Entry for the Table of Contents

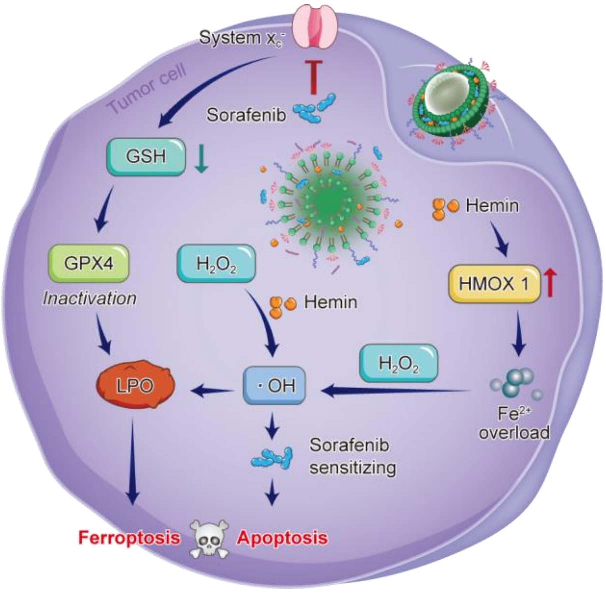

This research reports a pH-sensitive hybrid liposomal vesicle (SH-AD-L) based on amphiphilic dendrimer, DPPC, DSPE-PEG$_{2000}$, and cholesterol, with sorafenib and hemin co-encapsulation. Hemin synergizes with sorafenib to disturb redox homeostasis and amplify oxidative stress via triggering GSH depletion, iron overloading, and •OH production, which further induce efficient tumor suppression via synergistic ferroptosis - apoptosis for advanced hepatocellular carcinoma therapy.